

Design Optimization of Soft Sensory Fiber Networks using 3D Printing

David Hardman¹, Thomas George Thuruthel¹, Antonia Georgopoulou^{2,3}, Frank Clemens², Fumiya Iida¹

Abstract—The human tactile system is composed of multi-functional mechanoreceptors distributed in an optimized manner. Having the ability to design and optimize multi-modal soft sensory systems can further enhance the capabilities of current soft robotic systems. This work presents a complete framework for modelling, optimization and fabrication of soft sensory fiber networks for contact localization. The resistive sensor network is modelled using a novel geometric information theory based approach. We use genetic algorithms to optimize the strain sensor morphology and machine learning for contact localization. For precise and repeatable performances we use 3D printing technologies to manufacture our flexible sensory networks. Extensive simulation and experimental studies are performed on the optimized network in comparison with a baseline model. Our results show excellent sim-to-real match, tunable performances and good localization accuracy, even in the presence of damage and nonlinear material properties. The potential of the sensor network to function as a capacitive sensor is also demonstrated.

Index Terms—Soft Robotic Sensors; 3D Printing; Machine Learning;

I. INTRODUCTION

SOFT robotic sensing technologies have shown incredible developments in the last decade [1]. Their applications are wide and diverse, including the fields of soft robotics, wearable devices and human-machine interfaces. Although these novel technologies are promising, their usage has been limited by difficulties in fabrication, design and modelling: issues which are interdependent [2], [3]. This work combines novel developments in 3D printing flexible materials and information theoretics based design and modelling approaches to develop more accurate and robust sensory skins.

Functional materials used in the design of soft strain sensors include liquid conductors [4], [5], [6], nanocomposites [7], [8], [9], and optic fibers [10]. Fabrication and placement of these sensors typically involve direct moulding, injection moulding and/or manual placement. These processes introduce variability among the sensors. Additionally, these sensors suffer from highly nonlinear time-dependent effects. Depending on the strain responsive mechanism, this can be because of damage, rearrangement of conductive particles [11], geometric effects induced by the surrounding visco-elastic matrix, or delamination [12]. Precise and repeatable manufacturing techniques can

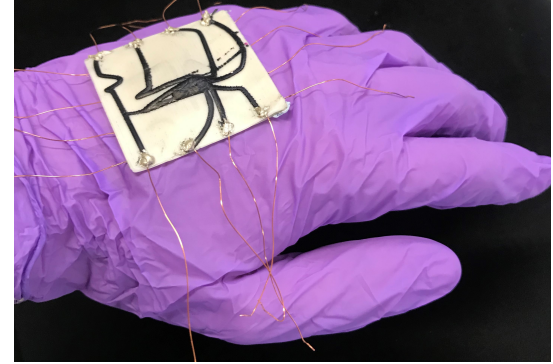


Fig. 1: An optimized and 3D printed sensor morphology functioning as a soft & flexible skin.

pave the way for reducing these nonlinear effects and studying their cause [13], [14]. 3D printing sensory structures is one of the ways to improve sensor properties [15], [16], [17], [18], [19], [20], [21]. 3D printing not only allows us to fabricate sensors in a consistent and repeatable manner but also allows us to develop complex sensor morphologies that are designed through optimization.

The role of sensor morphology and its application for the processing and structuring of sensory cues is a commonly observed phenomenon in nature and often applied in robotic sensors [22]. Two examples in nature are the facial whiskers of rodents [23] and the sensilla morphology of the crayfish antennular flagellum [24]. Similar concepts have been applied to soft robotic sensors: Culha et. al. used finite element models to find the optimal sensor morphologies for detecting kinematic parameters [25]. This work is an extension of the author's previous work on the design optimization of soft strain sensor morphologies that perform better in terms of robustness and accuracy [26], [27]. The previous research used information theory (IT) metrics to evaluate sensor morphologies rapidly using approximate deformation models without the need of accurate sensor models and performed common optimization techniques to improve their performance. The key insight was that these IT metrics are obtained independent from the actual physics and allow us to easily transfer the models onto real-world scenarios[28]. However, due to poor fabrication techniques, these optimized sensor networks had drastic sim-to-real differences.

This work shows that 3D printed soft sensors combined with simple geometrical sensor models can be used to develop optimized sensory skins with predictable performances (Figure 1). We perform extensive experimental studies to character-

¹ The Bio-Inspired Robotics Lab, Department of Engineering, University of Cambridge, UK.

² Department of Functional Materials, Empa – Swiss Federal Laboratories for Materials Science and Technology, Überlandstrasse 129, 8600 Dübendorf, Switzerland

³Vrije Universiteit Brussel (VUB), and Flanders Make Pleinlaan 2, B-1050 Brussels, Belgium

ize the sensor performance under normal circumstances and when damage occurs. Our results demonstrate how sensor morphology can be exploited to generate skins of varying tactile properties without the need for additional sensors or sensing modalities. We also investigate the applicability of our 3D printed sensory skins for capacitive sensing, in order to measure applied forces and provide additional redundancy to the network.

II. THEORY

In this section we briefly describe the modelling and design optimization approach for the soft sensory skin. A detailed overview can be found in [26]. A purely geometric model of the sensory skin is used for optimizing the sensory skin. Here we assume that the sensor response is just a function of the sensor geometry and the shape of the contact surface. As the information theory metric we use for estimating the performance of the sensor (obtained by numerical methods) is independent of the underlying function that transforms the sensor deformation to electrical signals, this assumption is reasonable. Any effect of stress concentration due to pre-strain, uneven material distribution or crosstalk is assumed to be negligible. Each sensor morphology is parameterized with N variables. The number of sensors in a grid is denoted by $2M$, where M is the number of sensors on each side. Each parameter corresponds to a point (with coordinates x, y) in space. Piecewise cubic hermite interpolation is used to derive the shape of the sensor from these N 2-D coordinates. Two examples of such sensory skins with 8 individual sensors can be seen in Figures 2 & 5, where the first square grid network is the most commonly used morphology for contact localization. Such morphologies are not ideal as for each location on the skin only two sensors will be active at a time, making it inefficient and more sensitive to damages.

Once the deformation shape and location of contact is known, the strain values in each sensor can be simulated with our geometric model. The model determines the strain values from the length of the sensor within the deformation area scaled by the inverse of its distance from the center of the deformation:

$$s_m = \sum_{p=1}^P \Delta d_p / dist_p \quad (1)$$

$$\forall m = 1 .. 2M$$

Here, Δd_p is the length of each numerically quantized segment within the deformation area, P is the number of quantized segments, and $dist_p$ is the distance of each segment from the deformation center.

Once each morphology is parametrized, we can evaluate them using numerical IT metrics. We use joint entropy as a measure of robustness to loss of sensory data. For non-redundant localization tasks (where the sensor distribution is sparse with respect to the contact area), increasing the joint entropy also results in an average increase in localization accuracy. The joint entropy of the simulated parametric model can be estimated by a short, continuous and uniform sampling of the response across the sensor area.

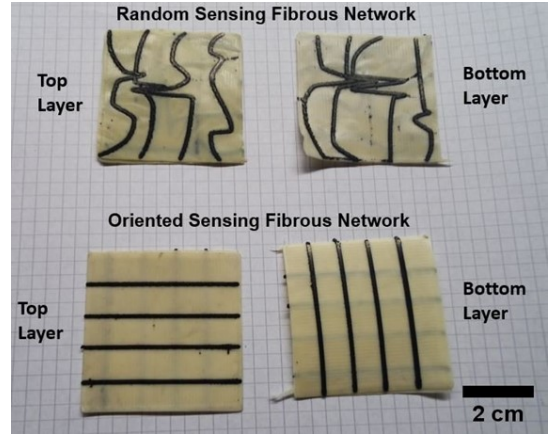


Fig. 2: The 3D printed sensing fiber networks, fabricated with pellet-based FDM for the optimized (top) and grid (bottom) geometry. The grid geometry is referred as morphology A and the optimized sensor is referred to as morphology B throughout this paper.

The sensor responses are stored and normalized. For Q samples from the sensor network of size $2M$, the joint entropy is measured as:

$$J.E = H(S_1, S_2, \dots, S_{2M}) \quad (2)$$

$$S_1 = [s^1, s^2, \dots, s^Q]$$

On top of optimizing the joint entropy ($J.E$) of the sensory skin, we add additional penalties on the cumulative area of sensor crossing (C) and the sharpness of the shapes (Z). The multi-objective optimization problem can be formulated as a minimization problem:

$$\min_z \alpha \frac{1}{J.E} + \beta Z + \gamma C \quad (3)$$

$$z = [(x_1, y_1), (x_2, y_2), \dots, (x_{2M}, y_{2M})]$$

$$x_{min} < x < x_{max}$$

$$y_{min} < y < y_{max}$$

in which α, β , and γ must be tuned to get the right trade-off between information content, learnability and ease-of-fabrication. We use a genetic algorithm for finding the optimal morphologies. For this work we test an optimized shape that is designed to be robust to damages (Figure 2).

III. FABRICATION

A. 3D printing of soft sensory fiber networks

For the piezoresistive sensing material, a styrene-based tri-block co-polymer (Kraiburg TPE, Germany) with shore hardness 50A is mixed with carbon black (Imerys, Switzerland) in a 1:1 mass ratio. The two materials are mixed by a torque Rheometer HAAKE Polylab Rheomix 600 (Thermofisher, Germany) and extruded into strands with a diameter of 1.75 mm using a capillary rheometer RH7 (NETZSCH, Germany). To achieve granulates with a length of 3 mm, the strand is cut manually.

Two sensing fiber network structures are printed using a pellet-based fused deposition modelling (FDM) method: One

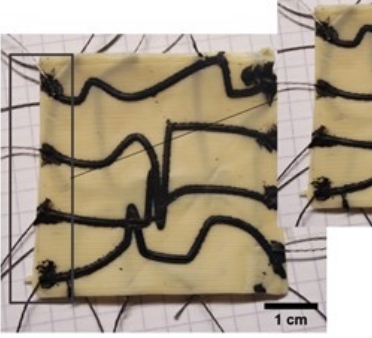


Fig. 3: Connection of the conductive yarn with conductive paste on the edge of 3D printed sensing fiber networks.

with the optimized morphology and another with a 4×4 grid. To be able to investigate the piezoresistive and capacitive sensing behaviours of the network, both structures are printed on a styrene-based tri-block co-polymer (Kraiburg TPE, Germany) elastomeric substrate, with shore hardness 68A.

The printing process is described in detail in a previous study [29]. In short, a pellet printer Voladora NX+ (International Technology 3D Printers, S.L, Spain) is used. First the elastomeric substrate is printed and on top the fiber network. A temperature of 230°C is used for the printing nozzle and 90°C for the printing bed. The printing speed is 30 mm/s and the extrusion multiplier is set at the value of 10. After printing, the two networks are laminated together by placing them in the oven for 30 minutes at 170°C. Figure 2 shows the fiber networks before the lamination process.

After the fabrication of the networks, a conductive yarn (Adafruit, USA) is used to connect the edges of the conductive pathways to the characterization setup. The connective yarn is fixed in place using a conductive paste (Bare Conductive, UK): Figure 3.

IV. SENSOR CHARACTERIZATION

Characterization of the sensor networks is undertaken using a Universal Robots UR5 robotic arm (Figure 4) to provide a series of controlled and precisely located presses across the surfaces of the two sensor morphologies. A PLA probe end effector is designed to provide a uniform pressure over a circle of diameter 5mm: 56% of the 9mm grid size. The centre of the probe can be sent to any point within a 25mm square characterization area, marked in Figure 5b. ‘A’ refers to the grid morphology, and ‘B’ to the optimized morphology.

The underside of each printed grid is secured onto 2mm thick EVA foam using VHB tape, and secured firmly to the table. The compressibility of this foam enables the probe to provide substantial local deformations to the grid, reproducing responses similar to those during use as a flexible skin on the surface of a soft material. Six locations within the characterization area are marked in Figure 5b - these are the probe locations used to generate the resistive and capacitive responses in later figures.

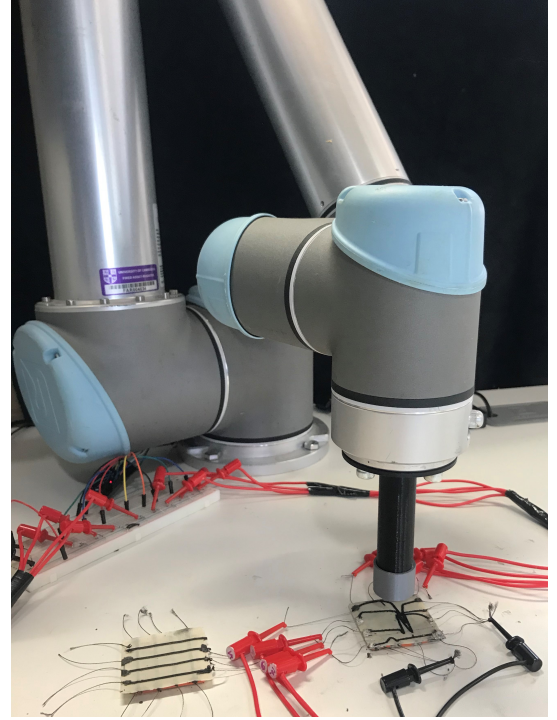


Fig. 4: The robotic arm setup for characterizing the sensor responses.

A. Resistive Response

Resistive responses are recorded across two sensors for each morphology, marked A1, A2, B1, B2 in Figure 5b. One end of each sensor is grounded, and the other coupled to +5V via a $1k\Omega$ resistor, creating a potential divider. The voltages at the central nodes of the dividers are sampled using the analog input pins of an Arduino Pro Mini microcontroller, sent via serial connection to a PC, and recorded using Teraterm logging software. Conversion to resistance is performed after measurements are taken, such that the logged values are quantised into the 10-bit resolution of the microcontroller at 10Hz. The magnitude of the sensor responses to two probed locations - (22.5, 22.5) & (14.5, 30.5) - is displayed in Figure 6a. Each probe is repeated 5 times, measuring the maximum deviation from the local baseline resistance, taken to be the average of the measured value directly prior to and after probing, in order to account for any small effects of transient drift.

Most notably, a sensor’s resistive response can be both positive and negative, depending on the probed location. Sensors in morphology A’s square grid most often increase in resistance when a deformation is applied, matching the assumptions used by the simulation - that local applied strains will impede the flow of current through the sensor. The sign of morphology B’s responses, as well as the magnitudes, can change with probe location: sensor B1 is seen to increase in resistance when centrally probed, whilst decreasing in resistance during offset probing. Noting the proximity of the offset location to the tight cluster of sensors in Figure 5b, and that the width of the channels in the printed samples leads to the connection

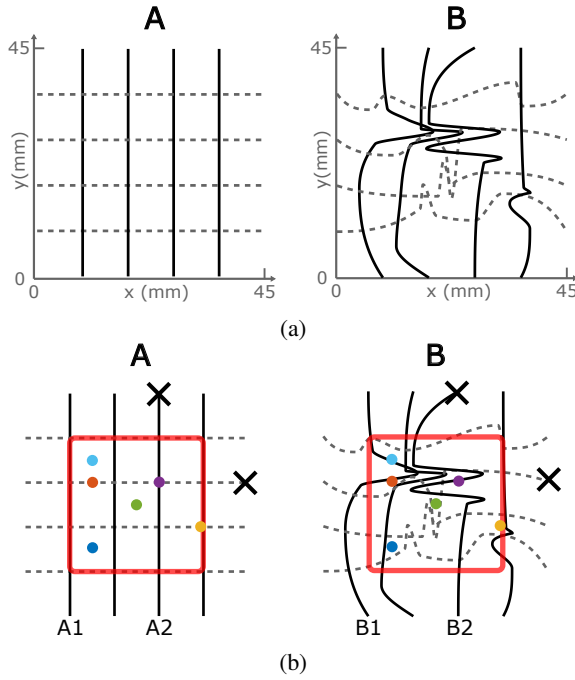


Fig. 5: (a) Schematics of the two printed sensor morphologies. Solid black lines indicate sensor channels which were uppermost during testing, and dashed grey lines those on the underside. (b) The characterization area (red) for all tests, and the probe/connection locations used to obtain resistive and capacitive responses.

of B1 & B2 in this area, we hypothesise that this decrease of resistance is due to the deformation's tendency to strengthen the connection between these channels, providing a path of lower impedance to ground regardless of which sensor is being sampled. Though not modelled by the simulation, this effect should not affect the performance of the network as long as the response is still a function of the length of the sensor fibers under deformation. The usage of IT metrics is hence vital here as it is practically impossible to analytically model the response of these sensor networks. Figure 6a's narrow error bars indicate the repeatability of both morphologies' resistive responses.

Figure 6b shows the step response of one sensor to five probes at (22.5, 22.5). Five decreases in resistance are clearly visible, with very little drift or overshoot. The responses are significantly larger than any background noise in the system and, as such, simple signal filtering can be applied to convert the response into a representative square wave.

B. Capacitive Response

The capacitive responses of each of the two morphologies are demonstrated by sampling the capacitance across the thickness of the insulating material. This is recorded using a Keysight U1731C LCR meter with a 1kHz probing signal, which sends measurements via serial connection to a host PC with a 1Hz sampling rate. The locations at which the meter's leads are attached to the morphologies are marked by crosses in Figure 5b. For each, four locations are probed five times

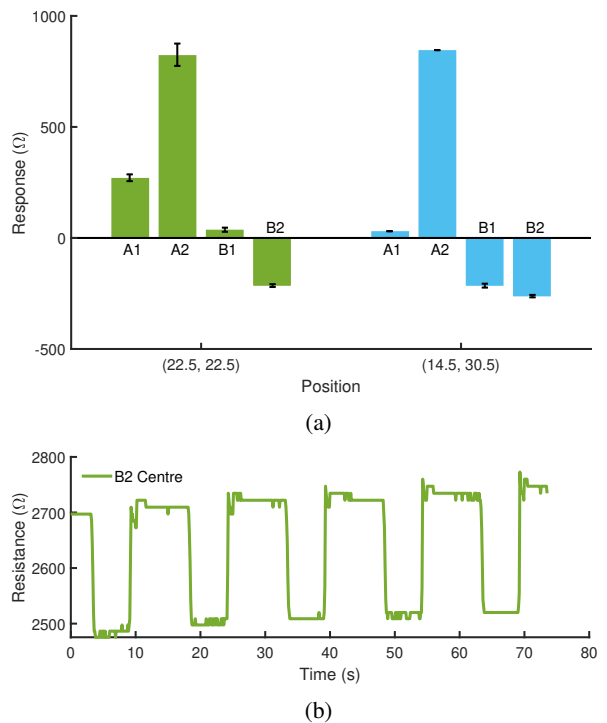


Fig. 6: (a) Relative magnitude of the resistive responses at central and offset probe locations. (b) A characteristic resistive response to 5 repeated probes.

- the relative magnitudes of the responses (see Section IV-A) are given in Figure 7a.

Given the thickness of the dielectric medium (0.4mm) and the small surface areas between sensors, the limited magnitudes of the responses ($\sim 10^{-13} F$) are unsurprising, and are 2 orders of magnitude lower than the baseline capacitances of the sensor/logging setup. Despite this, clear patterns arise from the 4 probed locations: particularly, optimized morphology B consistently returns responses of higher magnitude due to the increased surface area between the sensors acting as plates, compared to the small surface area (limited by the printed line widths) afforded between any two sensors in the square grid. At position (27, 27), this intersection is exactly probed, and the response of largest magnitude is returned. Morphology B's responses are greatest when the distance between probe and the tracked sensors is minimized, suggesting that, by combining a number of capacitive responses, the probed locations can be inferred. These results act as a proof of concept of the prints' abilities to perform as both resistive and capacitive sensors - combining the two types of measurement would provide further redundancy and robustness in the calculated probe locations by increasing the joint entropy, and could be simultaneously measured from the gain and phase shift of applied AC signals. Additionally, the capacitive response could be used to measure the magnitude of an applied force along with its contact location, measured using the resistive response. Figure 7b shows a characteristic capacitive response to 5 probes - the responses are clearly visible, though less separated from the background noise than the resistive responses of

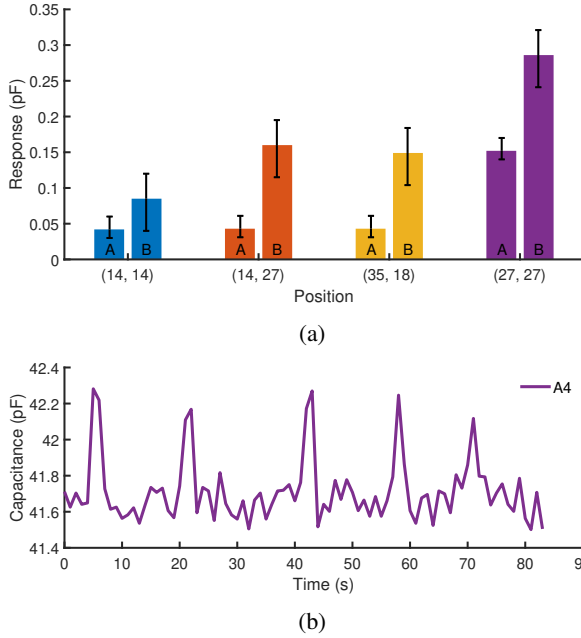


Fig. 7: (a) Relative magnitude of the capacitive responses at four probe locations. (b) A characteristic capacitive response to 5 repeated probes.

Figure 6b. Further developments of this optimization and fabrication method would seek to increase the effective signal-to-noise ratio by accounting for surface area in Equation 3, and by minimizing the dielectric thickness. All subsequent experimentation and results use the resistive responses of the two morphologies.

V. RESULTS

A. Undamaged Sensors

To compare the behaviours of the printed morphologies with the simulated responses, each is probed at 5000 random locations. The resistive responses of all 8 sensors are simultaneously recorded using the serially connected microcontroller introduced in Section IV-A. After preliminary testing to determine the best approach for training the neural networks, the signals are filtered using total variable denoising [30], [26], and all probed responses are converted to a set of 8 representative values using the same drift elimination approach discussed in the characterization methodology.

After splitting the 5000 data samples into 70:15:15% Training:Validation:Test sets, a separate 8-input \rightarrow 100-neuron hidden layer \rightarrow 2-output single layer neural network is trained using the Levenberg-Marquardt algorithm for each morphology. The subsequent errors in predicted location over all 5000 samples are plotted in Figure 8, normalized to the 9mm grid size. Both morphologies demonstrate similar behaviours to those of the simulations, indicating that the simulator's assumption of resistive dependence on local strain deformations is the effect most governing the sensor response. In morphology A, the effects of the grid are apparent, yielding areas of minimum error at the centre of the bounded squares

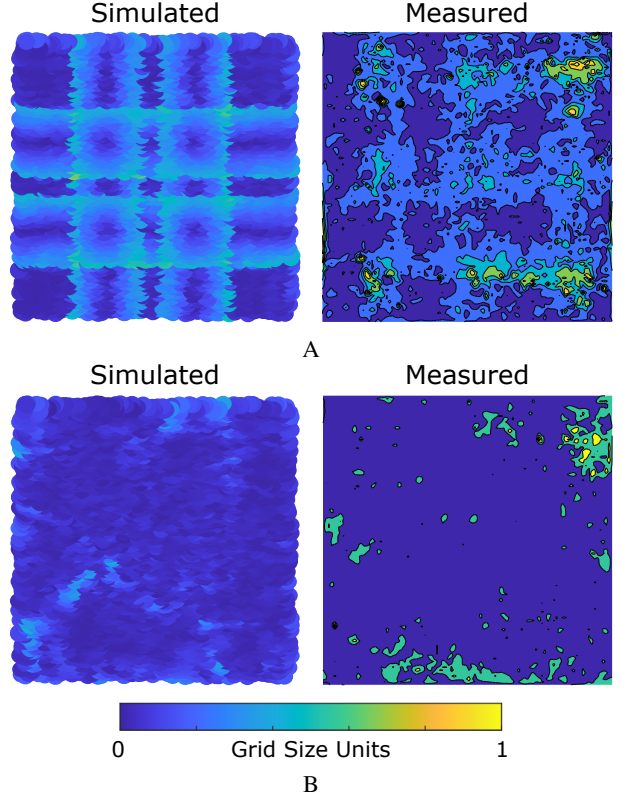


Fig. 8: Simulated and measured error distributions for the two sensor morphologies, over the 25 \times 25mm area marked in Figure 5b.

where there is most redundancy between the 8 responses, but higher errors around each sensor, where the grid's symmetry causes issues with localization. Conversely, there is no clear representation of the sensor morphology in the response of optimized grid B, with errors more uniformly distributed across the characterization area. Small clusters of higher error emerge at the edges of the area, particularly near the top right corner, where nearby sensors are relatively sparse. The first column of Table I indicates the mean and median error magnitude for both sensors. At ~ 2.5 mm, all of these values are remarkably small: $< \frac{1}{3}$ of the 9mm grid size, and $< \frac{1}{2}$ of the 5mm probe diameter. This demonstrates excellent performance of the material choice and fabrication method in producing unique and repeatable resistive responses.

Morphology B's network has a lower median error after training, reflecting its large consistently low-error areas containing only small regions of higher error. Morphology A has the lower mean error, though this is less uniformly distributed over the characterization area. By simultaneously measuring the capacitive responses to introduce more redundancy, we would expect to eliminate morphology B's higher errors and produce a fully uniform response, whilst the uncertainty in direction around A's symmetrical grid lines is more difficult to remove.

TABLE I: Mean and median error values for the 6 plots in Figures 8, 10, & 12.

	Undamaged	Damaged	Damaged + Retrained
$M_A(\text{mm})$	2.16	3.07	2.38
$M_B(\text{mm})$	2.01	3.53	2.46
$\mu_A(\text{mm})$	2.54	4.34	2.95
$\mu_B(\text{mm})$	2.65	4.82	3.28

B. Damaged Sensors

To evaluate the printed sensors' robustness to damage, we first examine a particular case in which one sensor from each side (marked in Figure 9) is broken and returns no response. Considering a sensory skin deployed in a soft robotic application, there are two damaged sensor scenarios to be considered: in the first, the controller is unaware of the damage, and continues to infer tactile predictions under the assumption that both sensors are still operational. In the second, the controller has detected the damage, and is able to recalibrate its response accordingly. For the first case, we examine the subsequent errors using the trained networks of Section V-A, simulating the damaged sensors by replacing their corresponding inputs with zeros during testing. The resulting error distributions, using the same scale as Figure 8, are given in Figure 10, with Table I's second column containing the mean and median error values. Despite a decrease in accuracy, all measured mean and median values remain impressively low, below the probe diameter. The optimized morphology has similar performance to the grid network for this sensor combination, though large regions of very low value errors are still prevalent throughout both distributions. Morphology A's main features match well between simulation and measurement, with the highest error regions occurring directly around the damaged sensors. The region of error in the lower right does not appear to have worsened from Figure 8, and may have arisen from an underperforming sensor during testing.

Though morphology B's error regions do not clearly align with those of Figure 10's simulations, the measured errors are mostly *lower* than those predicted, suggesting that the complex interplay and non-uniformity between the multiple channels produces a series of unique responses which were not modelled by the simulator's simple strain assumptions. Our ability to quickly 3D print and test new sensor morphologies allows these difficult-to-simulate advantageous effects to be exploited through physical optimization, an approach which is infeasible when the complex networks must be fabricated by hand.

To compare the robustness of the two morphologies, Figure 11 plots the average median error over all possible combinations of damaged sensors i.e. for n damaged sensors, $\binom{n}{n}$ combinations are considered and represented by a single bar in Figure 11. The two morphologies behave very similarly: optimized morphology B outperforms A for the $n = 0$ & $n = 3$ cases, whilst A averages a marginally better response when $n = 1$ & $n = 2$. Though this suggests that there is little reason to prefer one morphology based on these robustnesses, it is noted that morphology B's error bar minima are always lower than those of morphology A, a result which extends when

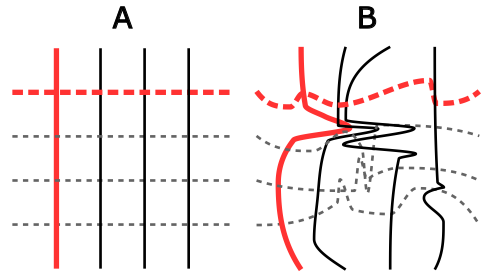


Fig. 9: The sensors assumed to be broken during simulation and physical experiments.

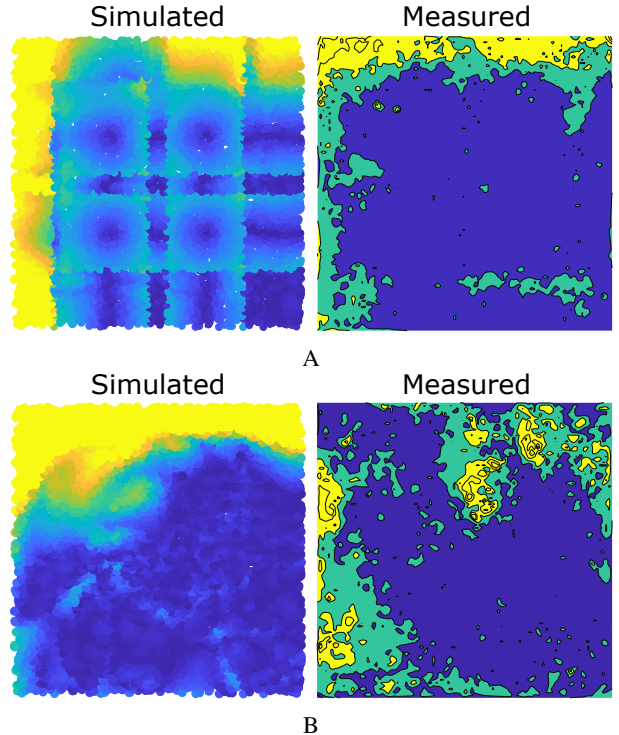


Fig. 10: Simulated and measured error distributions for the damaged sensor morphologies, before retraining of the neural networks.

retraining is performed for all $\{n \in \mathbb{N} \mid n < 8\}$ i.e. for a given n , the error distribution with lowest median error is always produced by optimized morphology B. This knowledge can be used to aid further development of sensor morphologies in which certain areas are more vulnerable to damage, such as the leading edge of a locomotive robot's soft skin.

The second damage scenario, in which the controller knows to neglect the damaged sensors, is presented in Figure 12. To produce this, Section V-A's neural networks are restructured and retrained with only 6 inputs: any responses of the two sensors marked in Figure 9 are ignored. In both cases, the controller is able to correct Figure 10's large error regions to produce large regions of low error: in many areas, the measured responses perform *better* than the simulation, indicated by darker blue regions.

As predicted by the simulation, the effect of errors is more localized and less symmetric in the optimized morphology.

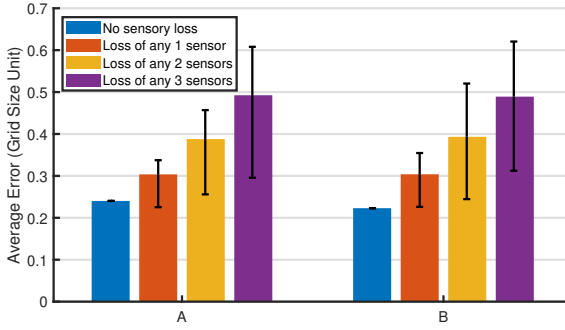


Fig. 11: Robustness of the two networks experiencing the damage of any combination of up to 3 sensors without retraining.

With 25% of sensors damaged, Table I indicates that both median errors increase by less than 0.5mm from the undamaged case, demonstrating the excellent sensory redundancy which Section III's fabrication method is capable of providing. To truly compare the networks' retraining capabilities, Figure 13 compares the median errors after retraining for any combination of up to three damaged sensors. Again, whilst neither morphology stands out as the best, morphology B's minima are less than those of morphology A for $\{n \in \mathbb{N} \mid n < 8\}$. Additionally, the average errors of all damaged sensor cases have decreased from Figure 11 after retraining; the highest average error reported in Figure 13 - 0.473 grid size units, or 4.26mm - is smaller than the diameter of the probe, demonstrating a high retainment of the sensors' locational accuracy even in the case of 37.5% total sensory damage. By coupling the trained networks with the sensors' capacitive responses, and by introducing mechanisms for damage detection and self-healing, these results pave the way towards the custom manufacture of truly universal soft sensory skins for wearables and soft robotics.

VI. CONCLUSION

The ability to easily fabricate complex resistive sensor morphologies through additive manufacturing enables us to optimize and tune the properties of sensory skins to particular applications, including areas of uniformly low error or particularly high redundancy. With measured error distributions demonstrating consistently similar patterns to those predicted by simulations, we have demonstrated the approach's potential to minimise the previously large reality gap faced when optimizing such morphologies.

The fabricated sensors can produce clean and repeatable tactile responses during measurements of resistance and capacitance, with minimal drift and overshoot. The combination of both sensitivity types shows promise in the design and production of sensors which are robust to significant damage, increasing redundancy with no corresponding increase in sensor complexity.

The governing strain-dependent resistive response mechanism observed in the measured sensors was the same as that assumed by the simple simulator, with a number of additional

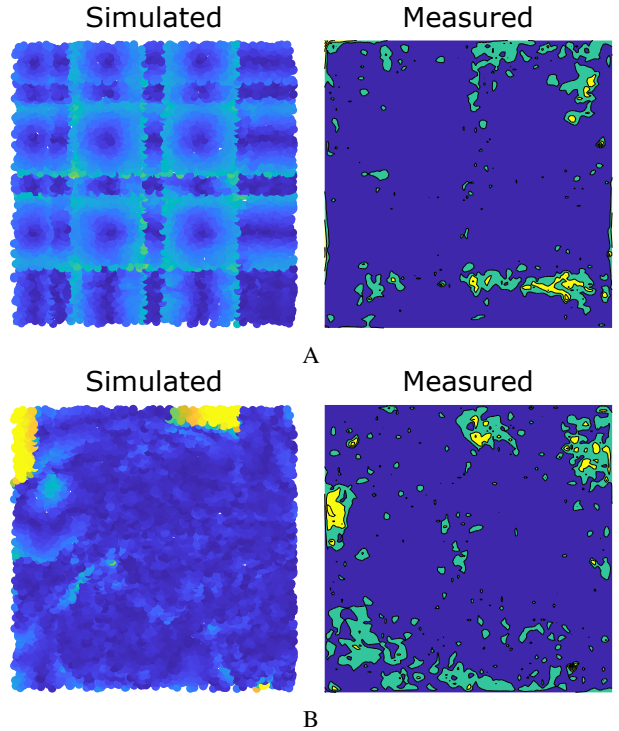


Fig. 12: Simulated and measured error distributions for the damaged sensor morphologies, after retraining of the neural networks.

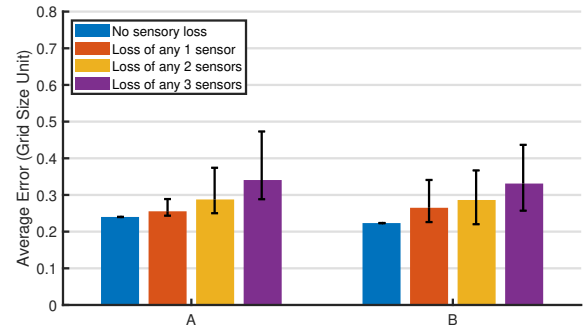


Fig. 13: Robustness of the two networks experiencing the damage of any combination of up to 3 sensors after retraining.

effects observed to emerge from crosstalk and from the sensor channel width. Though not included in the model, the non-uniform responses which these produced were advantageous to the neural networks, allowing them to infer the probed locations with remarkable accuracy and to often outperform the predicted results. The uniqueness of these sensory signals to particular areas of the optimized morphology provides a promising route for further development of multi-touch flexible sensory skins. Furthermore, the simplicity of our digital fabrication enables a quick way of testing these real-world effects for inclusion in the optimization process.

ACKNOWLEDGMENT

This work was supported by the SHERO project, a Future and Emerging Technologies (FET) programme of the

European Commission (grant agreement ID 828818), and by EPSRC DTP EP/R513180/1.

REFERENCES

- [1] M. Amjadi, K.-U. Kyung, I. Park, and M. Sitti, "Stretchable, skin-mountable, and wearable strain sensors and their potential applications: a review," *Advanced Functional Materials*, vol. 26, no. 11, pp. 1678–1698, 2016.
- [2] B. Shih, D. Shah, J. Li, T. G. Thuruthel, Y.-L. Park, F. Iida, Z. Bao, R. Kramer-Bottiglio, and M. T. Tolley, "Electronic skins and machine learning for intelligent soft robots," *Science Robotics*, vol. 5, no. 41, 2020.
- [3] H. Wang, M. Totaro, and L. Beccai, "Toward perceptive soft robots: Progress and challenges," *Advanced Science*, vol. 5, no. 9, p. 1800541, 2018.
- [4] R. K. Kramer, C. Majidi, R. Sahai, and R. J. Wood, "Soft curvature sensors for joint angle proprioception," in *2011 IEEE/RSJ International Conference on Intelligent Robots and Systems*. IEEE, 2011, pp. 1919–1926.
- [5] Y.-L. Park, C. Majidi, R. Kramer, P. Bérard, and R. J. Wood, "Hyper-elastic pressure sensing with a liquid-embedded elastomer," *Journal of micromechanics and microengineering*, vol. 20, no. 12, p. 125029, 2010.
- [6] S. Russo, T. Ranzani, H. Liu, S. Nefti-Meziani, K. Althoefer, and A. Menciassi, "Soft and stretchable sensor using biocompatible electrodes and liquid for medical applications," *Soft robotics*, vol. 2, no. 4, pp. 146–154, 2015.
- [7] C. Mattmann, F. Clemens, and G. Tröster, "Sensor for measuring strain in textile," *Sensors*, vol. 8, no. 6, pp. 3719–3732, 2008.
- [8] N. Hu, Y. Karube, M. Arai, T. Watanabe, C. Yan, Y. Li, Y. Liu, and H. Fukunaga, "Investigation on sensitivity of a polymer/carbon nanotube composite strain sensor," *Carbon*, vol. 48, no. 3, pp. 680–687, 2010.
- [9] A. Georgopoulou and F. Clemens, "Piezoresistive elastomer-based composite strain sensors and their applications," *ACS Applied Electronic Materials*, vol. 2, no. 7, pp. 1826–1842, 2020.
- [10] S. Sareh, A. Jiang, A. Faragasso, Y. Noh, T. Nanayakkara, P. Dasgupta, L. D. Seneviratne, H. A. Wurdemann, and K. Althoefer, "Bio-inspired tactile sensor sleeve for surgical soft manipulators," in *2014 IEEE International Conference on Robotics and Automation (ICRA)*. IEEE, 2014, pp. 1454–1459.
- [11] N. Hu, H. Fukunaga, S. Atobe, Y. Liu, J. Li, et al., "Piezoresistive strain sensors made from carbon nanotubes based polymer nanocomposites," *Sensors*, vol. 11, no. 11, pp. 10691–10723, 2011.
- [12] A. Georgopoulou, C. Kummerlöwe, and F. Clemens, "Effect of the elastomer matrix on thermoplastic elastomer-based strain sensor fiber composites," *Sensors*, vol. 20, no. 8, p. 2399, 2020.
- [13] T. G. Thuruthel, J. Hughes, A. Georgopoulou, F. Clemens, and F. Iida, "Using redundant and disjoint time-variant soft robotic sensors for accurate static state estimation," *IEEE Robotics and Automation Letters*, vol. 6, no. 2, pp. 2099–2105, 2021.
- [14] T. G. Thuruthel, B. Shih, C. Laschi, and M. T. Tolley, "Soft robot perception using embedded soft sensors and recurrent neural networks," *Science Robotics*, vol. 4, no. 26, 2019.
- [15] J. T. Muth, D. M. Vogt, R. L. Truby, Y. Mengüç, D. B. Kolesky, R. J. Wood, and J. A. Lewis, "Embedded 3d printing of strain sensors within highly stretchable elastomers," *Advanced materials*, vol. 26, no. 36, pp. 6307–6312, 2014.
- [16] T. Yang, D. Xie, Z. Li, and H. Zhu, "Recent advances in wearable tactile sensors: Materials, sensing mechanisms, and device performance," *Materials Science and Engineering: R: Reports*, vol. 115, pp. 1–37, 2017.
- [17] R. L. Truby and J. A. Lewis, "Printing soft matter in three dimensions," *Nature*, vol. 540, no. 7633, pp. 371–378, 2016.
- [18] A. K. Au, W. Huynh, L. F. Horowitz, and A. Folch, "3d-printed microfluidics," *Angewandte Chemie International Edition*, vol. 55, no. 12, pp. 3862–3881, 2016.
- [19] A. D. Valentine, T. A. Busbee, J. W. Boley, J. R. Raney, A. Chortos, A. Kotikian, J. D. Berrigan, M. F. Durstock, and J. A. Lewis, "Hybrid 3d printing of soft electronics," *advanced Materials*, vol. 29, no. 40, p. 1703817, 2017.
- [20] Q. Zhang, F. Zhang, S. P. Medarametla, H. Li, C. Zhou, and D. Lin, "3d printing of graphene aerogels," *Small*, vol. 12, no. 13, pp. 1702–1708, 2016.
- [21] D. Hardman, J. Hughes, T. G. Thuruthel, K. Gilday, and F. Iida, "3d printable sensorized soft gelatin hydrogel for multi-material soft structures," *IEEE Robotics and Automation Letters*, vol. 6, no. 3, pp. 5269–5275, 2021.
- [22] F. Iida and S. G. Nurzaman, "Adaptation of sensor morphology: an integrative view of perception from biologically inspired robotics perspective," *Interface focus*, vol. 6, no. 4, p. 20160016, 2016.
- [23] M. J. Pearson, B. Hutchinson, J. C. Sullivan, A. G. Pipe, and T. J. Prescott, "Biomimetic vibrissal sensing for robots," *Philosophical Transactions of the Royal Society B: Biological Sciences*, vol. 366, no. 1581, pp. 3085–3096, 2011.
- [24] S. Pravin, D. Mellon Jr, E. J. Berger, and M. A. Reidenbach, "Effects of sensilla morphology on mechanosensory sensitivity in the crayfish," *Bioinspiration & biomimetics*, vol. 10, no. 3, p. 036006, 2015.
- [25] U. Culha, S. Nurzaman, F. Clemens, and F. Iida, "Svas3: strain vector aided sensorization of soft structures," *Sensors*, vol. 14, no. 7, pp. 12 748–12 770, 2014.
- [26] T. G. Thuruthel, J. Hughes, and F. Iida, "Joint entropy-based morphology optimization of soft strain sensor networks for functional robustness," *IEEE Sensors Journal*, vol. 20, no. 18, pp. 10 801–10 810, 2020.
- [27] M. L. Visinsky, J. R. Cavallaro, and I. D. Walker, "Robot fault detection and fault tolerance: a survey," *Reliability Engineering and System Safety*, vol. 46, no. 2, pp. 139–158, 1994.
- [28] A. Krause, A. Singh, and C. Guestrin, "Near-optimal sensor placements in gaussian processes: Theory, efficient algorithms and empirical studies," *Journal of Machine Learning Research*, vol. 9, no. Feb, pp. 235–284, 2008.
- [29] A. Georgopoulou, L. Egloff, B. Vanderborght, and F. Clemens, "A sensorized soft pneumatic actuator fabricated with extrusion-based additive manufacturing," in *Actuators*, vol. 10, no. 5. Multidisciplinary Digital Publishing Institute, 2021, p. 102.
- [30] M. Little and N. Jones, "Generalized methods and solvers for noise removal from piecewise constant signals: Parts i and ii," *Proceedings of the Royal Society A*, 2011.